Effects of Ultraviolet Radiation on Sub-Neptune Exoplanet Hazes Through Laboratory Experiments

Lori Huseby, Sarah E Moran, Travis Barman, Tiffany Kataria, Sarah M. Hörst, Vishnu Reddy, Nikole Lewis, Véronique Vuitton

Draft version July 26, 2024
Typeset using LaTeX **twocolumn** style in AASTeX631

Effects of Ultraviolet Radiation on Sub-Neptune Exoplanet Hazes Through Laboratory Experiments

Lori Huseby,[1] Sarah E. Moran,[1] Neil Pearson,[1,2] Travis Barman,[1] Tiffany Kataria,[3] Chao He,[4] Sarah M. Hörst,[4] Cara Pesciotta,[4] Pierre Haenecour,[1] Vishnu Reddy,[1] Nikole K. Lewis,[5] and Véronique Vuitton[6]

[1] *University of Arizona, Lunar and Planetary Laboratory, 1629 E University Boulevard, Tucson, AZ 85721, USA*
[2] *Planetary Science Institute, 1700 E Fort Lowell Rd STE 106, Tucson, AZ 85719, USA*
[3] *Jet Propulsion Laboratory, 4800 Oak Grove Dr, Pasadena, CA 91011, USA*
[4] *Johns Hopkins University, 301 Olin Hall 3400 N. Charles Street, Baltimore, MD 21218, USA*
[5] *Department of Astronomy and Carl Sagan Institute, Cornell University, 122 Sciences Drive, Ithaca, NY 14853, USA*
[6] *Univ. Grenoble Alpes, CNRS, CNES, IPAG, 38000 Grenoble, France*

ABSTRACT

Temperate sub–Neptune exoplanets could contain large inventories of water in various phases, such as water–worlds with water–rich atmospheres or even oceans. Orbiting close to M–dwarf stars, these planets receive large amounts of radiation, especially during flaring events, which may strip away their atmospheres. Both space–based and ground–based observations have shown that many exoplanets likely contain photochemically–generated hazes. Haze particles are important for the potential generation of organic matter and may impact the evolution or origin of life. In addition, haze layers could provide a mechanism for lower atmospheric insulation and ultimately atmospheric retention. M–dwarf stars are known to have higher stellar activity than other types of stars, and stellar flares have the potential to accelerate atmospheric escape. In this work, we present results on laboratory investigations of UV radiation effects simulating two different stellar flare energies on laboratory–produced exoplanet hazes made under conditions analogous to water world atmospheres. We find that both simulated flares altered the overall transmittance and reflectance of the hazes, and higher energy flares make those alterations more pronounced. On a larger scale, these hazes diminish over the simulated flaring period. Our results provide important insight into the effects that stellar flaring events have on potential exoplanet haze composition as well as the ability for water world-like exoplanets to retain their atmospheres.

1. INTRODUCTION

Of the over 5500 confirmed exoplanets, the most common are considered super–Earths (1.25 – 2.00 R_{Earth}) or sub–Neptunes (2.0 – 4.0 R_{Earth}) (Borucki et al. 2011; Fressin et al. 2013; Fulton et al. 2017). In addition, these exoplanets frequently orbit the most common type of host star, M dwarfs (e.g.,Henry et al. 2019). Exoplanets orbiting M dwarfs could be notable targets for further atmospheric composition characterization, which could help us better understand the properties of these planets that our own Solar System does not have.

Both space–based and ground–based observations have shown that many exoplanets contain clouds and hazes in their atmospheres (e.g., Marley et al. 2013; Morley et al. 2013; Kreidberg et al. 2014; Knutson et al. 2014a,b; Dragomir et al. 2015; Libby-Roberts et al. 2020; Kreidberg et al. 2022). The resulting exoplanet atmosphere transmission spectra are more difficult to characterize when clouds and planetary hazes are present, as these cause larger than Rayleigh scattering slopes in optical wavelengths (e.g., Ohno & Kawashima 2020), and dampening of spectral features in the infrared wavelength region (e.g., Morley et al. 2013; Kreidberg et al. 2014; Knutson et al. 2014a,b; Dragomir et al. 2015; Libby-Roberts et al. 2020; Kreidberg et al. 2022). Of particular importance are planetary hazes, which continue to have poorly understood growth mechanisms and can widely affect observations. Planetary hazes are formed when gasses in an atmosphere are dissociated or ionized by high–energy radiation, undergo subsequent chemical reactions, and eventually form more chemically–complex, irreversible solids suspended in the

Corresponding author: Lori Huseby
lhuseby@arizona.edu

atmosphere (Gao et al. 2021). Planetary hazes vary widely in composition, shape, and size, which in turn changes the optical properties of the haze (Arney et al. 2016, 2017; Gavilan et al. 2018; Corrales et al. 2023; He et al. 2024).

Photochemical hazes are present across many bodies in the solar system, anywhere between the stratosphere and ionosphere (McKay et al. 1989, 1991; Wilson & Atreya 2003, 2004). The large bulk of our knowledge of haze chemistry stems from the Solar System through, for example, Titan's chemical abundances (Hörst 2017), alterations in Pluto's heating and cooling (McKay et al. 1989; Zhang et al. 2017), and atmospheric dynamic tracing of both Saturn and Jupiter (Sánchez-Lavega et al. 2016). More specifically, Titan's observed atmospheric haze is the result of photons and energetic particles interacting with the N_2 and CH_4 found in the moon's atmosphere, subsequently creating an efficient mechanism for organic photochemical haze production (Wilson & Atreya 2004; Lavvas et al. 2013; Hörst 2017; Gavilan et al. 2018).

Photochemical hazes were also present on early Earth. In the late Archean atmosphere of Earth (4.0 – 2.5 Gyr), an organic haze derived from biologically–generated CH_4, similar to a Titan–like haze, was intermittently present when the ratio of CH_4 to carbon dioxide would exceed 0.1 (Jacobson et al. 2000; Pavlov et al. 2001; Trainer et al. 2006; Arney et al. 2017). The subsequent haze–forming interactions along with incoming solar radiation had global climate impacts, including heating the Earth's stratosphere and potentially providing UV radiation shielding. Consequently, this haze contributed largely to the mechanism for thermal balance between the layers of Earth's atmosphere necessary for survival of land–based organisms (Jacobson et al. 2000; Arney et al. 2016, 2017). This haze layer therefore connects the biological and environmental evolution in Earth's history, and in addition, can provide a strong transport mechanism for organic material to the surface (Trainer et al. 2006; Arney et al. 2017; Pearce et al. 2024).

The initial photochemistry necessary to trigger planetary haze formation is likely to also be present in the atmospheres of exoplanets and create thousands of organic molecules with varying compositions (Hörst et al. 2018; He et al. 2020a; Moran et al. 2020; Vuitton et al. 2021). Recent laboratory studies and modeling campaigns have suggested that hydrocarbon and organic haze particles are produced predominately through photochemistry in temperate exoplanets with equilibrium temperatures less than 1000K (Crossfield & Kreidberg 2017; He et al. 2018b; Gao et al. 2020; He et al. 2020b,a; Yu et al. 2021; Brande et al. 2024). However, many exoplanets found in this temper[illegible]range, more specifically super-Earth and su[illegible]nets, have no solar system analogu[illegible]overall surface and atmospheric [illegible]anets much more unknown to us, a[illegible]n laboratory work on how these ha[illegible] to irradiation even more necessary

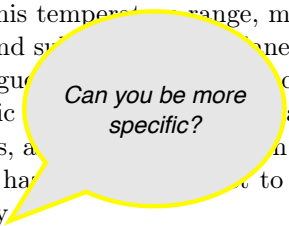

While there are photochemically–made hazes on many exoplanets, there are specific subsets of planets where they are present more often. More recent work after the initial discovery of the radius gap (Fulton et al. 2017) has attempted to better categorize the potential compositional differences between super–Earth and sub–Neptune exoplanets. Super–Earths have silicate-iron compositions, while sub–Neptune exoplanets have a different observed mass–radius relationship (Luque & Pallé 2022). This then suggests a difference in bulk density, where sub–Neptunes could have ice–silicate compositions, or thin hydrogen or helium envelopes (Mordasini et al. 2009; Kite & Ford 2018).

This difference in bulk density can mean a variety of compositions, some of which can include water. There is an increasing amount of evidence suggesting the existence of water–world exoplanets. A potential hypothesis is an ice-silicate bulk density mixture in combination with a close–in orbit and higher stellar radiation to create a temperate sub–Neptune exoplanet. Temperate sub–Neptune exoplanets could maintain liquid water on their surface, creating water worlds, or planets with water–rich atmospheres and oceans (Mordasini et al. 2009; Kite & Ford 2018; Kite & Schaefer 2021; Luque & Pallé 2022; Madhusudhan et al. 2023). Water is one of the key molecules for life on Earth that is sought out through spectral analysis of exoplanet atmospheres. Water vapor has been previously detected in the atmospheres of sub–Neptune exoplanets, for example TOI 270d (e.g., Benneke et al. 2024). Previous laboratory studies have also shown that water–rich atmospheres interact with high energy particles to result in organic haze formation (He et al. 2018b; Hörst et al. 2018; Moran et al. 2020; He et al. 2024).

Temperate sub–Neptune water world exoplanets that orbit close to their star can also be affected by stellar activity, and more specifically, stellar flares. Stellar flaring can impact planets around cool stars ($T_{\rm eff} \sim 3000$K), where the habitable zone (Kasting et al. 1993) is in close proximity to high energy stellar fluxes that are potentially harmful for orbiting planets (Rimmer et al. 2018; Howard et al. 2020). Flares occur when magnetic reconnection events heat localized regions of a stellar surface resulting in elevated radiation fluxes across most wavelengths (Hurford et al. 2003; Benz & Güdel 2010).

Flares are several orders of magnitude more luminous and more frequent than that of our Sun, releasing more high energy particles towards the exoplanets orbiting them (Benz & Güdel 2010).

Stellar flares can trigger photochemistry in both gaseous and terrestrial exoplanets (Grenfell et al. 2014; Rugheimer et al. 2015; Miguel et al. 2015). The increased photochemical reaction rates can alter the chemical composition and power chemical disequilibrium on an exoplanet atmosphere (Konings et al. 2022). In addition, stellar flares can drive water loss and atmospheric escape (e.g., Luger et al. 2015; Lin et al. 2019; Louca et al. 2023). Most of these sub-Neptune exoplanets have periods less than 100 days, where they are subject to high irradiation that can cause atmospheric mass loss, potentially stripping the planet from an atmosphere completely (Mordasini et al. 2009). Water worlds are particularly susceptible to atmospheric escape, specifically X–ray/extreme ultraviolet (XUV) escape. This mechanism dissociates the atmospheric water vapor, and the resulting atomic hydrogen escapes through hydrodynamic winds (Luger et al. 2015; Louca et al. 2023). However, photochemical hazes may have the potential to insulate the planet's atmosphere, providing a mechanism for thermal balance as in the atmosphere of early Earth. Hazes can also shield the lower atmosphere from high UV radiation, protecting a water–rich atmosphere and other important habitable biosignatures from further atmospheric mass loss Arney et al. (2016, 2017).

Critically, it remains unknown how stellar flaring affects exoplanet hazes. Previous laboratory work on oxidized Titan–like hazes that underwent UV irradiation revealed the formation of oxygenated bonds and new electronic transitions (Gavilan et al. 2018). Other laboratory work shows that hazes can contain many different prebiotic species within them, such as potential sugars, amino acids, and nucleotide bases (Moran et al. 2020). While the optical properties of organic hazes are needed to refine models of both Archean Earth (Haqq-Misra et al. 2008; Wolf & Toon 2010; Gavilan et al. 2018) and exoplanet atmospheric modeling, temperate sub-Neptune exoplanet haze molecular properties and changes over time are necessary to understand the spectral variations and persistence of such particles as a function of irradiation.

The aim of this work is to quantify spectral changes to exoplanet hazes as they are exposed to UV radiation simulating a higher energy event, and begin to understand if water world exoplanets would be able retain their haze layer and overall atmosphere. We subjected two laboratory–made "water world" haze samples to varying UV irradiation environments to assess how the hazes evolve over time. We measured the transmittance and reflectance spectra of the hazes before and after UV irradiation across a broad wavelength range (from Far Ultraviolet (FUV) to mid–IR, 0.2 – 15 μm), which overlaps with both HST and JWST instruments accessible for transiting exoplanet observations. This work will improve our understanding of haze evolution in sub–Neptune exoplanet atmospheres and our understanding of how stellar flares can impact the composition and atmospheric chemistry at work in these exotic worlds.

In Section 2 we describe our experimental methods including the physical haze production (2.1) and our haze UV bombardment process (2.2). Section 3 describes the findings of our experimental work, including the physical appearance of our samples in addition to transmittance (3.2), reflectance (3.3), and time–series results (3.5). In Sections 4 and 5 we discuss the implications of our results and their importance to the wider exoplanet science community.

2. EXPERIMENTAL METHODS

2.1. *Haze Analogue Production*

Photochemical hazes are expected to play an essential role in exoplanet atmospheres with equilibrium temperatures less than 1000K. In addition, atmospheres with increased metallicities, or increased atmospheric abundances of elements heavier than hydrogen and helium, will have photochemical hazes present (Gao et al. 2020). The detailed compositions of cool, high mean molecular weight exoplanet hazes are not well measured due to the complexities in which they are formed, which includes the breakdown of small molecules into radicals and ions, which then continue to react and build more complex molecules. The bulk laboratory haze compositions reflect the major gasses found in the atmosphere (Lavvas et al. 2013; Lavvas & Koskinen 2017; Gavilan et al. 2018; Gao et al. 2021). Therefore, we must rely on chemical equilibrium calculations in which inputs of exoplanet temperature, pressure, and metallicity are used to guide the atmospheric composition (Moses et al. 2013). These compositions provided a starting point for this experiment investigating the irradiation of photochemically–produced hazes in the atmospheres of sub–Neptunes.

The water world compositions were chosen by approximating 1000x solar metallicity, as motivated by previous laboratory experiments (He et al. 2018a,b; Hörst et al. 2018). These experiments found that laboratory hazes generated from high abundances of water vapor had high laboratory production rates at 300K (e.g., Hörst et al. 2018), a larger size distribution of the haze particles (e.g., He et al. 2018a), and that both CH_4 and CO con-

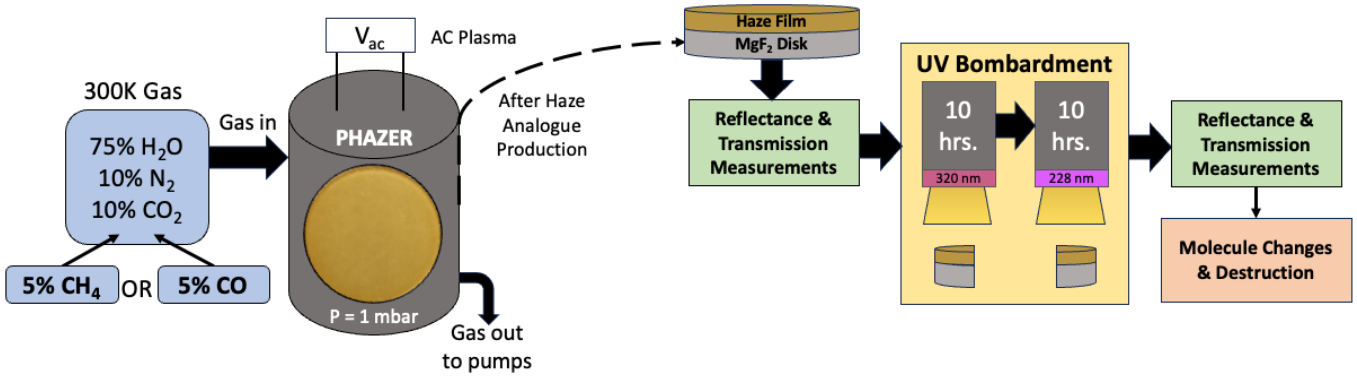

Figure 1. Streamlined schematic of the experimental setup, simulated atmospheric compositions and conditions, UV bombardment process, measurements, and experimental outcomes. Two laboratory hazes were produced (the initial conditions varying only in the minor carbon source) in the PHAZER chamber (He et al. 2017) by exposing the gas mixture at room temperature to an AC plasma source. After the hazes were produced, each half of the films were exposed to UV irradiation under two different filters. The transmittance and reflectance spectra pre– and post–UV irradiation of both samples were measured using a FTIR spectrometer in order to quantify molecular changes and destruction during the irradiation process.

taining hazes increased production rates in haze formation (e.g., Hörst & Tolbert 2014; Hörst et al. 2018). This experiment used 1000x metallicity as a starting point. However, due to the complexity of unknown parameters, we simplify the atmospheric compositions after our bulk H_2O contribution to the two major species of secondary outgassed atmospheres: CO_2 and N_2 (Deming & Seager 2017). Then, either CO or CH_4 was added at the 5% level to ensure that they will interact photochemically in an observable manner (Morley et al. 2013). This work will help investigate the role that the minor carbon source has in organic haze formation and resistance to simulated stellar flaring events.

Table 1. Gas compositions of the two samples made at 300K, 1 mbar. These two gas mixtures represent approximately equilibrium compositions at the previously mentioned 1000x metallicity, scaled slightly for experimental simplicity. The two haze samples differ in the minor carbon source. The physical hazes in this work were made to mimic a potential sub–Neptune water world atmosphere.

Sample 1	Sample 2
75% H_2O	75% H_2O
10% N_2	10% N_2
10% CO_2	10% CO_2
5% CO	5% CH_4

Table 1 breaks down the initial gas compositions used to make the two haze samples for this experiment. Two haze samples analogous to sub–Neptune water world atmospheres made from H_2O–dominated atmospheric mixes with varying carbon sources making up 5% of the representative atmosphere were produced at the Johns Hopkins University Planetary Haze Research (PHAZER) laboratory (He et al. 2017).

Here we briefly describe the haze production process guided by He et al. (2024) and further described in He et al. (2017); Hörst et al. (2018); He et al. (2020a). To prepare the film sample for this experiment, an optical–grade MgF_2 substrate plate (diameter: 25 mm, thickness: 1 mm, Crystran) was placed into the PHAZER chamber for sample collection. MgF_2 substrate plates were utilized as MgF_2 is chemically–inert and transparent in the wavelength range of 0.1 – 9 microns.

Gas mixtures, except for the water vapor, were premixed into a stainless–steel cylinder with high–purity gases purchased from Airgas (N_2 – 99.9997%, CO_2 – 99.999%, CH_4 – 99.999%, CO – 99.999%). The gas mixture flowed at a rate of 3.4 standard cubic centimeters per minute (sccm). Water vapor is introduced to the system at a pressure of 1.25 Torr provided from HPLC water (Fisher Chemical) at the 300K experimental temperature.

The gas mixture was then exposed to an AC glow discharge in the PHAZER reaction chamber, as seen in Figure 1. The AC glow discharge is not analogous to any planetary atmospheric mechanism, like lightning for example, or stellar phenomenon, like a coronal mass ejection, but rather representative of energetic processes happening in the upper atmosphere. By utilizing this method, the AC glow discharge is able to dissociate stable molecules without altering the ambient gas temperature found in the chamber. This discharges electrons into the gas composition flow, which initiated the chemical processes necessary to form solid particles and new gas–phase products. The newly formed solid particles settled down the chamber onto our MgF_2 substrates as

thin films. The AC discharge exposure continued for 72 hours and was then turned off. The samples were then kept under vacuum for 48 hours to remove any volatile components.

After the vacuum purge and return to ambient pressure, the PHAZER chamber was transferred to a dry (<0.1 ppm H_2O), oxygen free (<0.1 ppm O_2), N_2 glove box (Inert Technology Inc.) at Johns Hopkins University to collect the haze products with no exposure to the Earth's atmosphere. The haze products were then stored and kept stable for 8 months protected from Earth ambient atmosphere and light sources. This storage period has previously been shown not to affect PHAZER samples, with particles maintaining their original compositions (Moran et al. 2022). We note that the energy density used in the AC plasma source (He et al. 2020a,b) was 170 W/m^{-2}, much higher than the quantitative flux received by temperate exoplanets orbiting M dwarf stars in quiescence (e.g., GJ 1214b $\sim$3.5W/m^2). This is due to the fact that laboratory simulations usually use a higher energy density to accelerate the chemical process in order to analyze and observe the chemical impact within a reasonable timeline (e.g., He et al. 2024). After haze production and between experiments, the haze products were kept in an N_2–purged box under aluminum foil wrapping to avoid contamination from light sources and Earth's atmosphere.

2.2. *FTIR Spectroscopy Measurements and Calculations*

2.2.1. *FTIR Measurements and UV Bombardment*

During the irradiation process, all measurements were performed at room temperature and held stable at 294K within the FTIR lab setup. The transmittance and reflectance of each sample prior to irradiation were taken in a monitored N_2–purged system (99.999%, AirProducts) at room temperature using a Nicolet iS 50R Benchtop Fourier Transform Infrared (FTIR) spectrometer (University of Arizona, Tucson, AZ), where we obtained spectra between 0.2 – 25 μm with 0.09 cm^{-1} maximum resolution.

For reflectance from 0.2 to 0.6 μm, we used an Avantes silicon spectrometer (University of Arizona, Tucson, AZ) with a deuterium lamp light source and silicon detector. From 0.37 to 1 μm in both reflectance and transmittance, we took 200 scans with a Si-diode detector and quartz beamsplitter and quartz–tungsten halogen lamp. From 1 to 5 μm in reflectance and transmittance, we took 200 scans with a Mercury Cadmium Telluride (MCT) detector and quartz beamsplitter and a quartz–tungsten halogen lamp. From 1.5 to 15 μm in reflectance and transmittance, we took 200 scans with a MCT detector and KBr beamsplitter and a globar light source. Overlap between detectors allowed for calibration between wavelength regions. In reflectance, we used a Spectrolon polytetrafluoroethylene (PTFE) standard from 0.2 to 5 μm and a gold standard was used for reference between 10 to 25 μm. All transmittance measurements were compared against a blank MgF_2 substrate plate identical to the haze product sample plate. UV–to–visible (200 – 800 nm) measurements were taken throughout the bombardment process (described below) every 1.5 hours using the Avantes spectrometer with 5 scans for a 1.4 nm resolution to monitor compositional changes over time.

The samples were then irradiated with two different bandpasses of light (215 – 245 nm, Peak: 228 nm, 20% throughput; and 320 – 380 nm, Peak: 350 nm, 80% throughput, respectively) for 10 hours per filter to simulate the effect of M dwarf host star flaring on an exoplanet atmospheric haze. One side of the sample was bombarded with UV light (Aventes Avalight DH–S–BAL Balanced Deuterium Lamp, Power: 78 W, Wavelength Range: 215–550 nm) through the 320 nm filter, and then subsequent transmittance and reflectance measurements were taken. Then the sample was rotated and bombarded with a UV lamp through the 240 nm filter with the same measurements taken as the other filter. This ensured that there would be no cumulative irradiation effects on the sample. The output of our UV light during the irradiation period is 1.1 W/m^2. The filters had different peak wavelength throughputs in order to compare a representative higher and lower energy flare impacting the atmosphere of the planet in the UV region. After each irradiation filter, transmittance and reflectance measurements were completed again to observe any changes due to the UV bombardment.

2.2.2. *Irradiated Sample Post–Processing*

For the UV-Vis data in transmittance and reflectance, clear outliers were removed (e.g. 484.23 nm – 487.15 nm, 654.66 nm – 656.95 nm). After the removal of the clear outliers, interference fringes were observed between 35000 – 18000 cm^{-1} (0.28 – 0.53 μm) in the time–dependent visible wavelength data. These interference fringes occur only in optical wavelengths due to multiple reflections between different film thicknesses across the sample (Neri et al. 1987). We applied the correction in Equation (1) following the moving average method of Neri et al. (1987) as used in He et al. (2022) and Moran et al. (2022) to eliminate the effect of the fringes. This procedure normalized the absorbed power by the transmitted power with assumptions that 1) the processed spectrum has equally spaced data points, and 2) that

the fringes have similar amplitudes. This correction follows the form:

$$F(X_n) = \frac{2G(X_n) + G(X_{n+m}) + G(X_{n-m})}{4}. \quad (1)$$

Here, X_n is the nth abscissa, $F(X_n)$ is the fringe-removed spectrum value at X_n, $G(X_n)$ is the original spectrum value at X_n, $G(X_{n+m})$ and $G(X_{n-m})$ are the original spectrum values at shifted abscissae and $2m$ is the maximum integer number of points contained in the interval d, which is the average fringe spacing. For our transmittance and reflectance spectra, the average fringe spacing (d) was approximately 2700 – 3000 cm^{-1} depending on sample and there are (1336 – 1500) points (m = 678 – 728) contained in the interval d. The reflectance and transmittance spectra in the near—infrared and thermal–infrared were not treated because they are unaffected by fringing. Once the removal of the interference fringes was completed, we then compared the spectra between pre– and post–UV irradiation across both filters.

3. RESULTS

3.1. *Haze Analogue Films*

We took images of our experimental haze analogues post–irradiation to show differences in the physical haze color between the two samples. Figure 2 shows composite images of the haze analogues and one of a MgF_2 blank (25mm diameter) as reference. The haze samples are yellow/orange in color, with the 5% CH_4–derived haze sample being slightly darker than the 5% CO–derived haze sample.

Previous studies (e.g Hörst et al. 2018; He et al. 2018b,a) have shown that darker colors in similar temperature hazes are due to haze production rate differences in addition to compositional changes. This could mean that the 5% CH_4 sample had a higher production rate as compared to the 5% CO sample. However, this is outside the scope of this work and will be explored in complementary studies by a subset of our team. More work is necessary to determine the complex chemical processes that produce the resulting color changes, and the implications they have for planetary haze production mechanisms. Pre–irradiation images are unavailable in order to limit atmospheric contamination with the haze analogues as the imager was not under N_2 purge. During the irradiation process, no physical color changes are seen by eye. Both haze analogues have a smooth surface, with a post–irradiation surface roughness of 17.67 nm for the 5% CO–derived haze sample and 3.08 nm for the 5% CH_4–derived haze sample. The spectral feature determinations are made following the IR spectrum tables from Sigma Aldrich in addition to previous laboratory work from e.g., He et al. (2022, 2024).

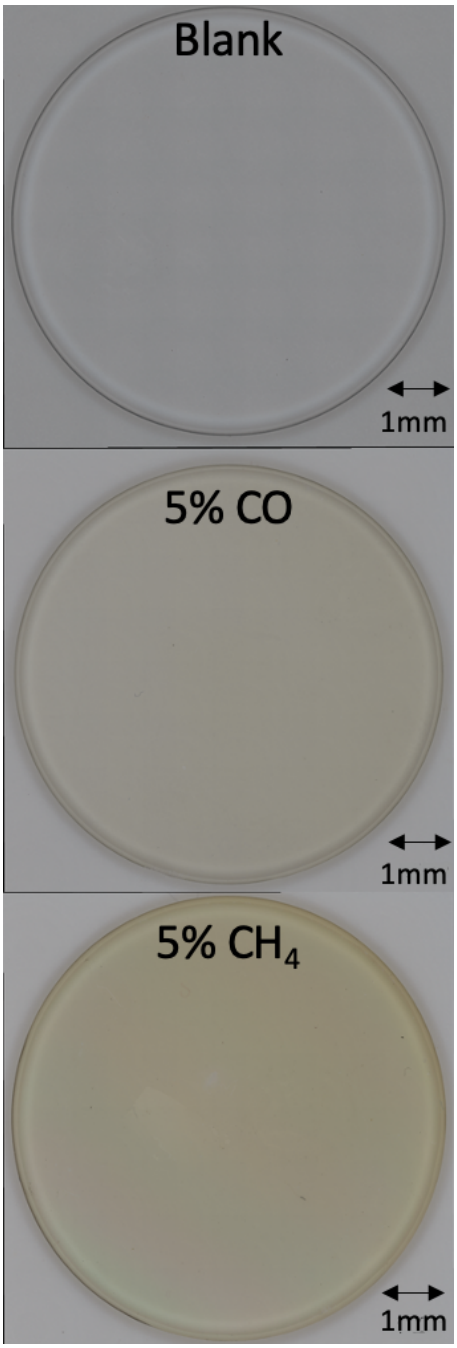

Figure 2. Composite images of the post-irradiation water world hazes deposited onto MgF_2 substrate disks (Diameter: 25mm). The image labeled blank is of a clean MgF_2 substrate disk. The image labeled 5% CH_4–derived haze sample is more yellow in color than the image labeled 5% CO–derived haze sample, indicating the differing composition and haze–forming efficiency of the samples.

3.2. *Transmittance Spectra Results*

Exoplanet atmospheric transmission observations, which are obtained in the transit characterization technique as the planet passes in front of the host star, can be altered by many different components, including hazes. Radiative transfer models require the opacities of hazes to understand their impact on exoplanet transmission spectra. Haze opacities can be calculated from the refractive indices of haze samples, derived from transmittance and reflectance spectra, as we measure here. Figure 3 shows the transmittance spectra of both samples pre– and post–irradiation.

We stitch together three different spectra from 0.37 – 1 μm, 1 – 5 μm, and 1.5 – 15 μm to make the full continuum in transmittance. As seen, the general spectral shape and features are similar throughout the irradiation process. While there were no optical fringes seen in either transmittance or reflectance using the FTIR instrument from 0.4 to 1 micron, there were two larger absorption features at 0.44 μm and 0.8 μm in both samples. This suggests that there may be larger aromatic compounds or other organic pi bonds present in the haze samples (Krevelen & Nijenhuis 2009). The spectrum is relatively featureless from 0.8 μm to 2.5 μm. However, the continuum increases as wavelength increases. Larger spectral features that can be distinguished are found from 2.5 to 9 μm as is typical of organic material (He et al. 2018b).

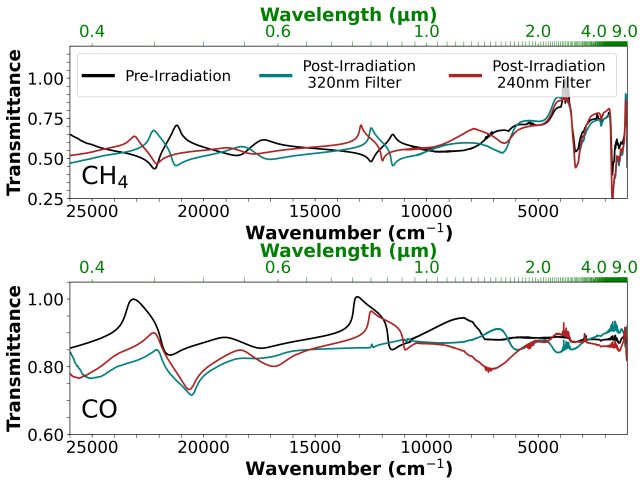

Figure 3. Transmittance spectra of our 5% CH_4 atmosphere haze sample (top) and 5% CO atmosphere haze sample (bottom) in the visible to mid–IR wavelength region (26000 – 1100 cm^{-1}, 0.4 – 9 μm). The black line represents the samples before the irradiation process began, and the teal and red lines represent the post–irradiation spectrum using the 320 nm and 240 nm filters respectively.

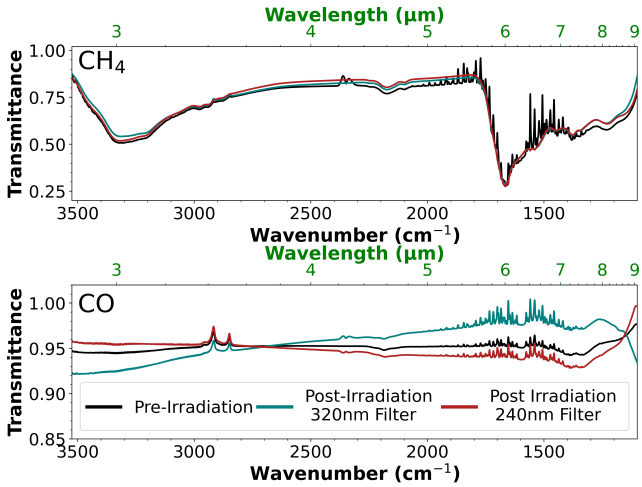

Figure 4. Enlarged spectrum between 3500 – 1100 cm^{-1} (2.5 – 9 μm) of the 5% CH_4 (top) and 5% CO (bottom) atmosphere haze samples as a function of wavelength in transmittance.

In Figure 4 we enlarge the spectrum between 3500 – 1100 cm^{-1} (2.5 – 9 μm) for closer inspection of spectral features indicative of particular molecular functional groups. For the 5% CH_4 atmosphere haze sample in transmittance, Table 2 identifies the bonds responsible for each spectral feature. There are characteristic bonds of O–H, C–H, C=O, C–O, and N–H bonds. We note that the spectra above 9 μm could be affected by the substrate disk that we used, as the transmittance of the disk at those wavelengths is near zero, meaning that small differences including noise may cause large spectral differences, which is why we exclude these longer wavelengths from our analysis. The large absorption feature between 3350 – 3200 cm^{-1} (2.97 – 3.12 μm) is largely due to O–H stretching, which is indicative of intermolecular bonded alcohols in this haze analogue, in addition to N–H amine stretching. Both of the filters increase the overall transmittance of the sample over this absorption feature, meaning that there are less O–H bonds present on the film. One mechanism could be that O–H bonds of the CH_4–derived haze sample have dissociated and recombined with other molecules to create more complex alcohols at a different wavelength, or dissociated completely, leading to an increase in transmittance found in the transmittance spectra.

There are two different peaks at 2925 cm^{-1} (3.42 μm) and 2850 cm^{-1} (3.51 μm) both indicating the presence of C-H stretching due to alkanes present in the haze analogue. During the irradiation process, both features again show an increase in transmittance, or an absorption loss of that spectral feature. This is similar to the 5% CO atmosphere haze sample, although the 5% CH_4

atmosphere haze sample has larger changes during irradiation. Figure 5 shows this continuum–like change. More specifically, the spectra across the 320 nm filter not only showed an increase in transmittance but had more substantial absorption feature peaks as compared to both the pre–irradiation spectrum and the spectra across the 240 nm filter. In the spectrum across the 240 nm filter, the doublet feature is not apparent, meaning that the higher energy radiation eliminates the spectral feature that occurs due to the C–H stretching. This potentially means that the large amounts of C–H bonds in the haze analogue have been fully dissociated due to the higher energy radiation.

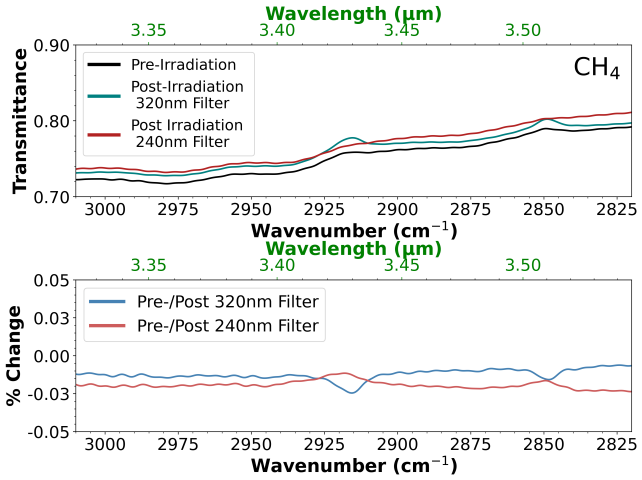

Figure 5. Top: the C–H stretching representative of an alkane spectral feature of the 5% CH_4 atmosphere–derived sample pre– and post–UV irradiation in transmittance. The post–irradiation through the 320 nm filter had larger increases in transmittance and created "bumps" in the spectra. Bottom: the percent change of the sample due to the UV bombardment

There is a strong, sharp doublet peak between 2375 – 2325 cm^{-1} (4.21 – 4.3 μm) attributed to a O=C=O stretch corresponding to carbon dioxide. The irradiation process made the spectrum more flat, where carbon dioxide could then be fully dissociated and the spectral features change to be an increase in the continuum instead. There are also more absorption features between 1800 – 1050 cm^{-1} (5.50 – 9.55 μm) range. This would be considered the fingerprint region of the spectrum, where a combination of organic molecules and various stretching and bending modes are present. The fingerprint region is highly complex, but it is also unique to each combination of molecules. This can better help determine the molecular structure of the haze sample pre– and post–irradiation. There is a large drop in the transmittance of the sample between 1800 – 1500 cm^{-1} (5.50 – 6.50 μm) due to a combination of C=C and C=O stretching. In the pre–irradiation spectrum, there is a hyper–fine structure present due to water contamination creating noise in that wavelength range. However, post–irradiation measurements across both filters do not have this same noise feature present. Between 1100 – 1050 cm^{-1} (9.10 – 9.55 μm), there were larger percent changes in the C–O stretch spectral feature during irradiation than in the rest of the spectrum. During irradiation across the 320 nm spectrum, there is a 0.12% difference between pre– and post–irradiation. This is much larger than in the 240 nm filter, where only a 0.08% difference is seen. For this specific spectral feature, the lower–energy simulated flare creates a larger increase in transmittance, meaning that less C–O stretching is present. We conclude that a potential proposed mechanism of the decrease in C–O stretching may be the dissociation of CO, CH_4, and water vapor during the irradiation process, then recombination with each other to create more complex organics for example, or total dissociated of these bonds into the surrounding ambient atmosphere.

In the 5% CO atmosphere haze sample in transmittance, Table 3 identifies the bonds responsible for each spectral feature. There are characteristic bonds of O–H, C–H, C=O, C–O, and N–H bonds. Overall, there are not large changes between the pre–irradiation spectrum and the post–irradiation across the 240 nm spectrum. There are larger changes across the 320 nm spectrum. The continuum has a lower transmittance longward of 2700 cm^{-1} (3.6 μm), and then increases in transmittance until approximately 1350 cm^{-1} (7.5 μm). After this point, noise increases reaching the transmittance edge of the MgF_2 disk. In addition, the total transmittance of the laboratory haze is between 88% to 100%, which is a much narrower range compared to the 5% CH_4 atmosphere haze sample. This is potentially due to the fact that the CO derived haze sample is a much thinner film compared to the CH_4 derived haze, in addition to any compositional differences between the two samples.

One distinction between the two samples is that there is no large absorption feature corresponding to an O–H stretch. The O–H stretch is largely present in the 5% CH_4 derived haze sample, but not present in the 5% CO derived haze sample. One potential mechanism for this is the CH_4 sample more readily dissociates (e.g., 360 kJ/mol or 0.33 μm; Cottrell 1954) under the influence of far-ultraviolet (FUV, 0.1350 – 0.1750 μm) radiation, while CO bonds require higher energies (e.g., 1072kJ/mol or 0.111 μm; Cottrell 1954) to be broken. The dissociated CH_4 creates excess hydrogen for other

Table 2. Spectral features and corresponding functional groups identified in the 5% CH_4– derived atmospheric haze sample pre– and post–irradiation in transmittance and reflectance. Spectral Features with an * are seen in both spectra.

Transmittance

Frequency (cm^{-1})	Wavelength (μm)	Functional Group (bond, type)	Intensity	% Change (240 nm, 320 nm)
3350 – 3200	2.97 – 3.12	*O–H alcohol (intermolecular bonded)	strong, broad	no change, ↑ 0.07%
3400 – 3225	2.95 – 3.10	*N–H stretching (amine group)	medium, broad	↓ no change, ↓ 0.07%
2925 – 2850	3.42 – 3.51	*C–H stretching (alkane)	medium, doublet	↑ 0.02%, ↑ 0.03%
2375 – 2325	4.21 – 4.3	*O=C=O stretching (carbon dioxide)	strong, doublet	↓ 0.03%, ↓ 0.05%
2175	4.63	C=N stretching (conjugated)	strong, broad	↑ 0.05%, ↑ 0.03%
1800 – 1500	5.50 – 6.50	C=C / C=O stretching	strong, broad	↓ 0.65%, ↓ 0.65%
1620 – 1580	6.2 – 6.35	N–H bending (amine)	medium, broad	↓ 0.1%, ↓ 0.1%
1100 – 1050	9.10 – 9.55	*C–O stretching (alcohol)	strong, broad	↑ 0.06%, ↑ 0.12%

Reflectance

3500 – 2700	2.86 – 4.0	*O–H stretching (alcohol/carbonic acid)	strong, broad	↓ 0.35% , ↓ 0.38%
3400 – 3225	2.95 – 3.10	*N–H stretching (amine group)	medium, broad	↓ 0.35%, ↓ 0.38%
3075 – 3025	3.25 – 3.30	*C–H stretching	medium, broad	↓ 0.3%, ↓ 0.3%
2740 – 2700	3.66 – 3.70	C–H stretching (aldehyde, doublet)	medium, sharp	↓ 0.38%, ↓ 0.33%
2362	4.23	*O=C=O stretch (carbon dioxide)	strong, sharp	↓ 0.44%, ↓ 0.42%
2329	4.29	O=C=O stretching (carbon dioxide)	strong, sharp	↓ 0.48%, ↓ 0.43%
2260 – 2222	4.42 – 4.5	C≡N stretching (nitrile group)	weak, broad	↓ 0.4%, ↓ 0.4%
1740 – 1700	5.75 – 5.87	C=O stretching (aldehyde)	strong, broad	↓ 0.42%, ↓ 0.42%
1675 – 1640	5.96 – 6.06	C=O, C=N, or C=C stretching	weak, broad	↓ 0.3%, ↓ 0.3%
1425 – 1375	7.0 – 7.25	C–H bending (aldehyde)	medium, sharp	↓ 0.58%, ↓ 0.61%
1275 – 1220	7.85 – 8.17	C–O stretching (ether group)	strong, broad	↓ 0.75%, ↓ 0.67%
1170 – 1130	8.52 – 8.85	C–O stretching (tertiary alcohol)	weak, sharp	↓ 1.02%, ↓ 0.75%
1085 – 1050	9.28 – 9.53	*C–O stretching (primary alcohol)	strong, sharp	↓ 2.2%, ↓ 1.5%

molecules to recombine with to form more complex O–H bonds. There are two different peaks at 2925 cm^{-1} (3.42 μm) and 2850 cm^{-1} (3.51 μm), both indicating the presence of C–H stretching due to alkanes present in the haze analogue. During the irradiation process, the higher–energy filter increases the transmittance of the spectral feature, while the lower–energy filter decreases the spectral feature. This is similar to the 5% CH_4 atmosphere haze sample, although the 5% CH_4 atmosphere haze sample shows larger percent changes during irradiation.

There is a strong, sharp doublet peak between 2375 – 2325 cm^{-1} (4.21 μm – 4.3 μm) which we attribute to a O=C=O stretch from carbon dioxide. In the pre–irradiation sample, the spectral feature is hardly seen. However, post–irradiation the spectral feature is more noticeable. Across the 320 nm filter spectrum, both the feature and the continuum increase. Across the 240 nm filter, the feature also increases, but the continuum is decreasing, leading to less transmittance across the spectral feature than that of the 320 nm filter. Therefore, higher–energy flares degrade the continuum more. However, spectral features may be present in the post–irradiation spectrum where they were not seen pre–irradiation (e.g, Figure 5 from 2950 – 2825 cm $^{-1}$ or 3.42 – 3.52 μm). One large difference between the two sample spectra is that there is no large drop in transmittance between between 1800 – 1500 cm^{-1} (5.50 – 6.50 μm). In the 5% CH_4 atmosphere haze sample, the large drop is due to both C=C and C=N stretching. While the 5% CO atmosphere haze sample has the same associated noise present, both of those spectral features are not present. This may be due to a lack of dissociation between the C=O bonds, which need significantly more energy to dissociate as compared to the C–H bonds found in CH_4 atmosphere haze. Instead, the largest drop is between 1390 – 1320 cm^{-1} (7.25 – 7.66 μm), where O–H bending rather than stretching is present. Across this spectral feature, the 320 nm filter increases across the spectrum, whereas it decreases across the 240 nm filter. Both of these changes seen can be attributed to the overall continuum decrease rather than any specific

Table 3. Spectral features and corresponding functional groups identified in the 5% CO–derived atmosphere haze sample pre– and post–irradiation in transmittance and reflectance. Spectral features with an * are seen in both spectra.

Transmittance

Frequency (cm^{-1})	Wavelength (μm)	Functional Group (bond, type)	Intensity	% Change (240 nm, 320 nm)
2925 – 2850	3.42 – 3.51	*C–H Stretching (alkane)	medium, doublet	no change, ↓ 0.02%
2375 – 2325	4.21 – 4.3	*O=C=O stretching (carbon dioxide)	strong, doublet	no changes
2175	4.63	C=N stretching (conjugated)	strong, broad	no changes
1620 – 1580	6.2 – 6.35	N–H bending (amine)	medium, broad	↓ 0.02%, ↑ 0.03%
1390 – 1320	7.25 – 7.66	O–H bending (alcohol)	weak, broad	↓ 0.02%, ↑ 0.03%
1150 – 1075	8.72 – 9.36	*C–O stretching (alcohol)	strong, broad	↑ 0.02%, ↓ 0.05%

Reflectance

3125 – 3075	3.2 – 3.25	O–H alcohol (intramolecular bonded)	weak, broad	no change, ↓ 0.04%
2925 – 2850	3.42 – 3.51	*C–H stretching (alkane, alkene)	medium, shoulder	no change, ↓ 0.03%
2329	4.29	*O=C=O stretching (carbon dioxide)	strong, sharp	no change, ↓ 0.03%
2260 – 2222	4.42 – 4.5	C≡N stretching (nitrile group)	weak, broad	no changes
1875 – 1845	5.32 – 5.42	C=O stretching (anhydride)	medium, sharp	↑ 0.03%, ↓ 0.02%
1740 – 1700	5.75 – 5.87	C=O stretching (aldehyde)	strong, broad	no changes
1460 – 1415	6.85 – 7.06	C–H bending (alkane, methyl group)	medium, broad	no change, ↓ 0.05%
1275 – 1220	7.85 – 8.17	*C–O stretch (ether group)	strong, broad	no change, ↓ 0.05%

spectral features, indicating a general degradation of the haze overall rather than any specific functional group destruction.

3.3. *Reflectance Spectroscopy Results*

Figure 6 shows the reflectance spectra of both samples pre– and post–irradiation. We stitch together three different spectra from 0.37 – 1 μm, 1 – 5 μm, and 1.5 – 15 μm to make the full continuum in reflection. As seen, the general spectral shape and features are similar throughout the irradiation process. The spectrum across both samples are relatively flat and featureless from 0.4 to 2.5 μm. The continuum stays flat as well with no increasing or decreasing slopes. We note that both the thickness of the haze films and the chemical compositions of the films impact the reflectance measurements in this experiment. We do see more spectral features appear between 2.5 to 9 μm due to various organic functional groups found in the exoplanet haze analogues. This is seen in Figure 7. The results are broken down by sample.

In the 5% CO atmosphere haze sample, Table 3 identifies the bonds responsible for each spectral feature. There are characteristic O–H, C–H, C=O, C–O, C=N, and C=C bonds, as with the transmittance measurements. The overall reflectance of the sample is between 0% to 6%. The absorption feature between 3500 – 3000 cm^{-1} is largely due to O–H bond stretching, with a small contribution from a N–H amine stretch. This is a weak,

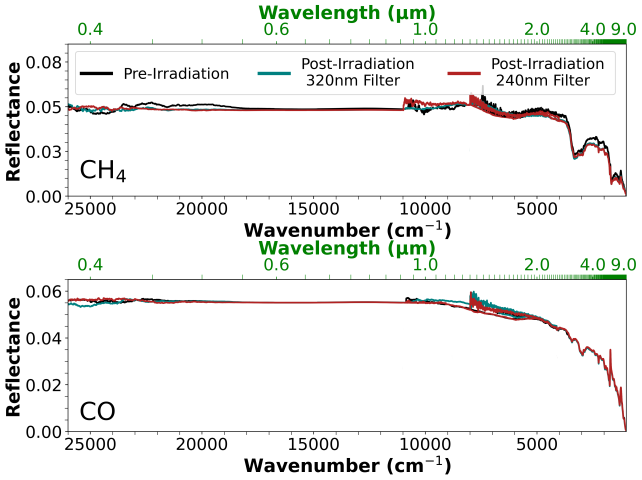

Figure 6. Reflectance spectra of our 5% CH_4–derived haze sample (top) and 5% CO–derived haze sample (bottom) in the visible to mid–IR wavelength region (26000 – 1000 cm^{-1}, 0.4 – 9 μm). The black line represents the samples before the irradiation process began, and the teal and red lines represent the post–irradiation spectrum across the 320 nm and 240 nm filters respectively.

broad feature that indicates intramolecular bonded alcohols. Both of the filters degrade the spectral feature during the irradiation process. The stretching of C–H between 2925 – 2850 cm^{-1} is present as well in sharper peaks in the spectrum. There is a strong, sharp peak at 2329 cm^{-1} attributed to an O=C=O stretch of carbon

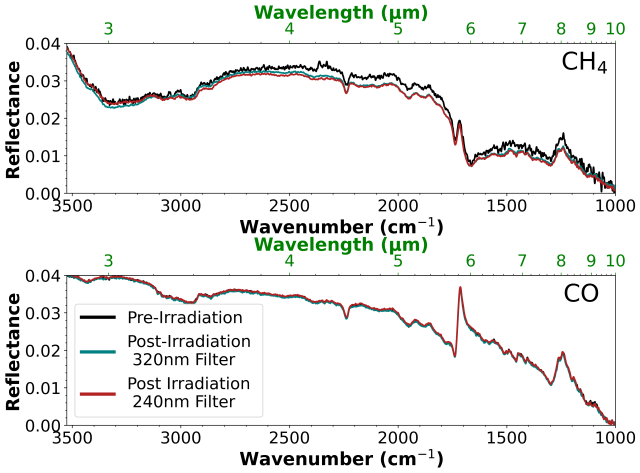

Figure 7. Enlarged spectrum between 3500 – 1000 cm^{-1} (2.5 – 10 μm) of the 5% CH_4 (top) and 5% CO (bottom) atmosphere generated hazes as a function of wavelength in reflectance. Between pre– and post–irradiation, there are larger changes in the 5% CH_4 derived haze spectrum in comparison to the 5% CO derived haze spectrum.

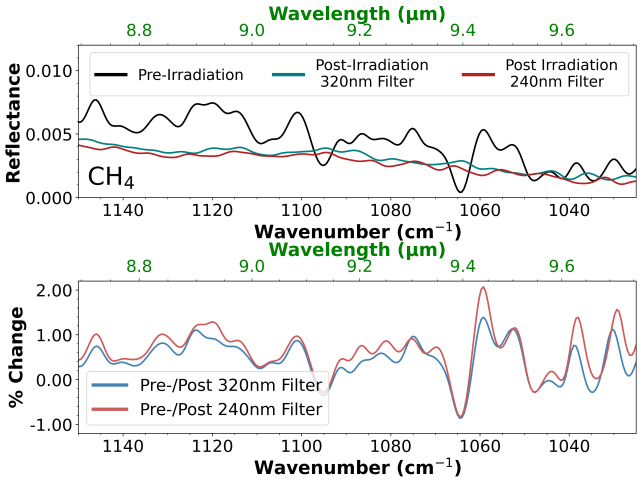

Figure 8. C–O stretching features of the 5% CH_4 derived haze sample evident of a primary alcohol seen pre– and post–irradiation in reflectance (top) with percent change (bottom) between pre–irradiation and post-irradiation of each filter respectively. The irradiation process degraded the spectral features across both filters.

dioxide. The two large peaks in the sample between 1740 – 1700 cm^{-1} and 1275 – 1220 cm^{-1} are C=O and C–O stretches, respectively, indicate the presence of complex organics. The C=O stretch feature remains unchanged during the irradiation process, however, the C–O stretch decreases under the 320 nm filter by 0.07%. Other absorption features in the spectrum indicate the presence of nitriles, aromatics, and organic groups. Largely the 240 nm filter increases the spectral feature across the haze analogue, and the 320 nm filter decreases the spectral feature across the haze analogue. The differences during irradiation between the two filters lead to distinctive compositional changes. These spectral and compositional changes will alter the resulting effectiveness of the haze in insulating the planetary atmosphere from the high radiation events of stellar flaring.

In the 5% CH_4 atmosphere haze sample, Table 2 identifies the bonds responsible for each spectral feature. There are characteristic features of O–H, C–H, C=O, C–O, C=N, and C=C bonds as seen in the 5% CO atmosphere haze sample. The large absorption feature between 3400 – 2700 cm^{-1} is due to O–H stretching, which is indicative of both alcohols (3500 – 3200 cm^{-1}) and carbonic acids (3300 – 2700 cm^{-1}) in this haze analogue. Within this feature there are also both N–H (3400 – 3225 cm^{-1}) and C–H (3075 – 2700 cm^{-1}) bond stretching respectively. Both of the filters decrease the spectral features during the irradiation process. There are two different peaks at 2362 cm^{-1} and 2329 cm^{-1}, both indicating the presence of O=C=O stretching due to carbon dioxide in the haze analogue. This is different from the 5% CO sample, which only has one peak. There are also more absorption features between 1740 – 1050 cm^{-1} range than the 5% CO sample. During the irradiation process, both filters decrease these spectral features across the spectrum. Of particular interest is the C–O bond stretching between 1085 – 1050 cm^{-1} seen in Figure 8. There are large changes between pre– and post–irradiation, and the spectrum across both filters decreases to a flat spectrum for a 2% change in the 240 nm filter and a 1.5% change in the 320 nm filter. This indicates a compositional change in the haze analogue, and a potential mechanism for degradation of water world hazes during stellar flaring events.

3.4. *Transmittance and Reflectance Summary*

As shown, there are more spectral features seen in the reflectance spectra of both samples in comparison to transmittance. There are also more spectral features seen in the 5% CH_4 derived haze sample than the 5% CO derived sample. This means that the laboratory haze samples are compositionally different.

In both transmittance and reflectance, large stretches of O–H, C–H, O=C=O, and C=N bonds are present in the 5% CH_4 derived haze sample. There are more distinguishable features in the reflectance spectrum as compared to transmittance, which may be due to the fact that reflectance spectroscopy enhances weak features that may not be seen in transmission spectroscopy. We also see more C–O, C=O, and C–H stretching in the reflectance spectrum, as many of these stretches may be

present in transmission, but are overshadowed by larger features.

In both transmittance and reflectance, large stretches of C–H, O=C=O, and C–O bonds are present in the 5% CO derived haze sample. In this case, the number of spectral features seen between reflectance and transmittance are approximately equal. However, there are some features that do not match between spectra, which may be due to the stretching bands being shifted to higher wavenumbers in reflectance.

As shown, there are also more spectral features seen in the 5% CH_4 derived haze sample than the 5% CO derived sample. This means that the laboratory haze samples are compositionally different not only between the two different derived haze samples, but also pre– and post–irradiation. This has key implications in the retainability of water world exoplanet hazes and how UV energy can change them over short timescales.

3.5. *UV-Vis Time Dependent Results*

3.5.1. *CO–Derived Haze Sample*

In addition to pre– and post–irradiation spectra, we also obtained UV-visible reflectance data every 1.5 hours throughout the experiment during bombardment. Figure 9 shows the pre– and post–irradiation spectra of the 5% CO atmosphere haze sample in reflectance for the ultraviolet–to–visible region.

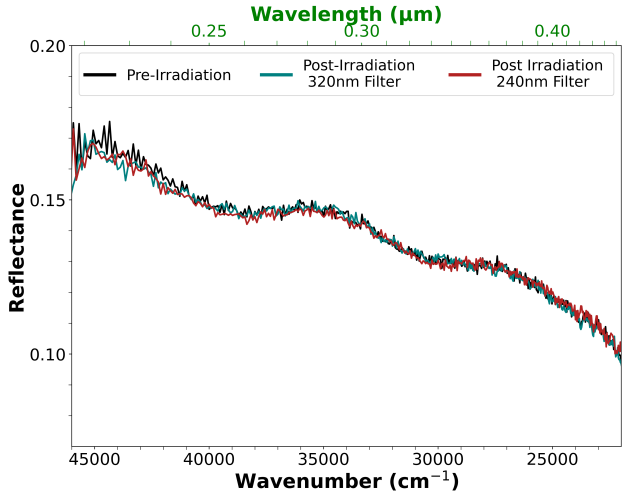

Figure 9. UV-visible (46000 – 18000 cm^{-1}, 0.23 – 0.46 μm) spectrum for the 5% CO atmosphere haze sample. Due to the apparent thinness of the haze film, there is no fringing seen. There are little to no changes between pre– and post–irradiation in this wavelength range.

The sample appears to be much thinner than the 5% CH_4 atmosphere haze sample based upon the post–irradiation magnified images (Figure 2), so only slight interference fringes are seen. Due to the limited amount of fringes and lack of large amplitudes they were not corrected for in the analysis. In addition, the potential interference fringes do not change during the irradiation process. In the UV–visible wavelength region, there are no large changes during the irradiation process for the 5% CO–derived haze sample. This is significantly different than the 5% CH_4–derived haze sample.

3.5.2. *CH_4–Derived Haze Sample*

The 5% CH_4–derived sample began as a thicker film based upon the post–irradiation magnified images, and interference fringes are present both pre– and post–irradiation. We show this both in Figure 10, which corresponds to the 320 nm filter, and Figure 11, which corresponds to the 240 nm filter.

During the irradiation process, the interference fringes observed change between pre– and post–irradiation in both filters. Since the interference fringes shift to shorter wavelengths, we infer that the actual thickness of the haze film changes post–irradiation. This means the irradiation process physically alters the haze layers present on the MgF_2 plate. This is also apparent with continuum changes in the infrared region both in reflectance and transmittance (e.g., Figure 4, 7).

Figure 10 shows the time-series data throughout the irradiation process for the CH_4–derived haze sample across the 320 nm filter. After correcting for the optical fringes as described in Equation 1, the corrected spectra were plotted as a function of wavelength. Due to the large amplitude changes towards longer wavelengths, the corrected data becomes noisier as wavelength increases. The spectra is flat throughout the irradiation process, and no specific spectral features can be pointed out. In order to see any potential changes in the overall reflectance of the sample, we investigate the corrected reflectance at 0.51 μm. This is plotted over time at the bottom panel of Figure 10 with the individual points connected in blue to better clarify the trend of the reflectance over time. We find that the reflectance decreases over time, from 7.8% reflective to 6.8% reflective. There is a gradual loss of reflectance over the first 9 hours of irradiation, and then it drops off more steeply as we reach the end of the irradiation process. This 1% loss in reflectance suggests that our sample became less reflective over the irradiation process, leading to an increase in transmittance, as it became a thinner film.

Figure 11 shows the time-series data throughout the irradiation process for the CH_4–derived haze sample across the 240 nm filter. After correcting for the optical fringes as shown for the 240 nm filter using the same steps as was shown for the 320 nm filter described

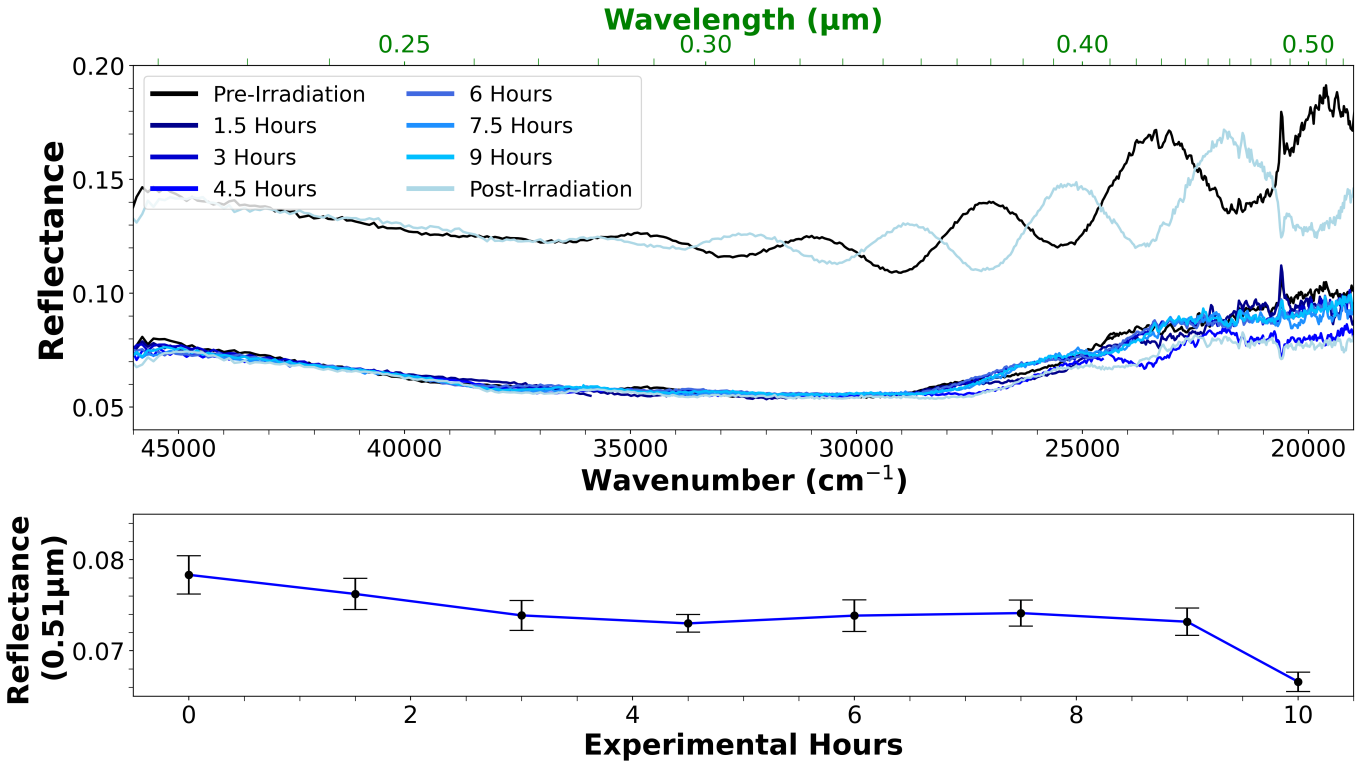

Figure 10. Top: UV-visible (46000 – 18000 cm^{-1}, 0.22 – 0.54 μm) spectrum for the 5% CH_4 atmosphere haze sample across the 320 nm filter, corrected for interference fringe effects. The pre– and post–irradiation uncorrected spectra have been offset vertically 6.5% for clarity. The corrected data during the irradiation process are plotted as is. Bottom: The reflectance of the fringe–corrected data plotted for a specific wavelength (0.51 μm) over the duration of the irradiation process. The error bars for the reflectance changes seen at 0.51 μm are derived from propagating error throughout the instrument and fringe interference equation.

above, the corrected spectra were plotted as a function of wavelength. We find that the reflectance decreases over time, from 7.9% reflective to 6.6% reflective. There is a steep loss in reflectance immediately starting the irradiation process, which then flattens out after 2.5 hours until the end of the irradiation process. This contrasts the trend found in Figure 10, where it was a more gradual loss of reflectance over time. Instead, after 2.5 hours, we reach the same reflectance as post–irradiation. This 1.3% loss in reflectance suggests that our sample became less reflective over the irradiation process, leading to an increase in transmittance, and also became a thinner film. In comparison, the total loss of reflectance across the 320 nm filter was only 1%, whereas the higher energy simulated flare from the 240 nm filter had a total loss of 1.3%, suggestion a further decrease of the amount of haze present on the disk.

We conclude that the simulated flare in this work decreased the thickness of our film, and if we apply this to our planetary analogue, decreased the amount of haze present in a water world atmosphere via destruction. In addition, the higher energy flare analogue decreased the thickness of our film more, which suggests any haze in an analogous atmosphere would decrease more as well. Our observed change in film thickness has large implications as this suggests that stellar flaring may have a large effect on atmospheric hazes, and could strip away the associated haze from the atmosphere of an water

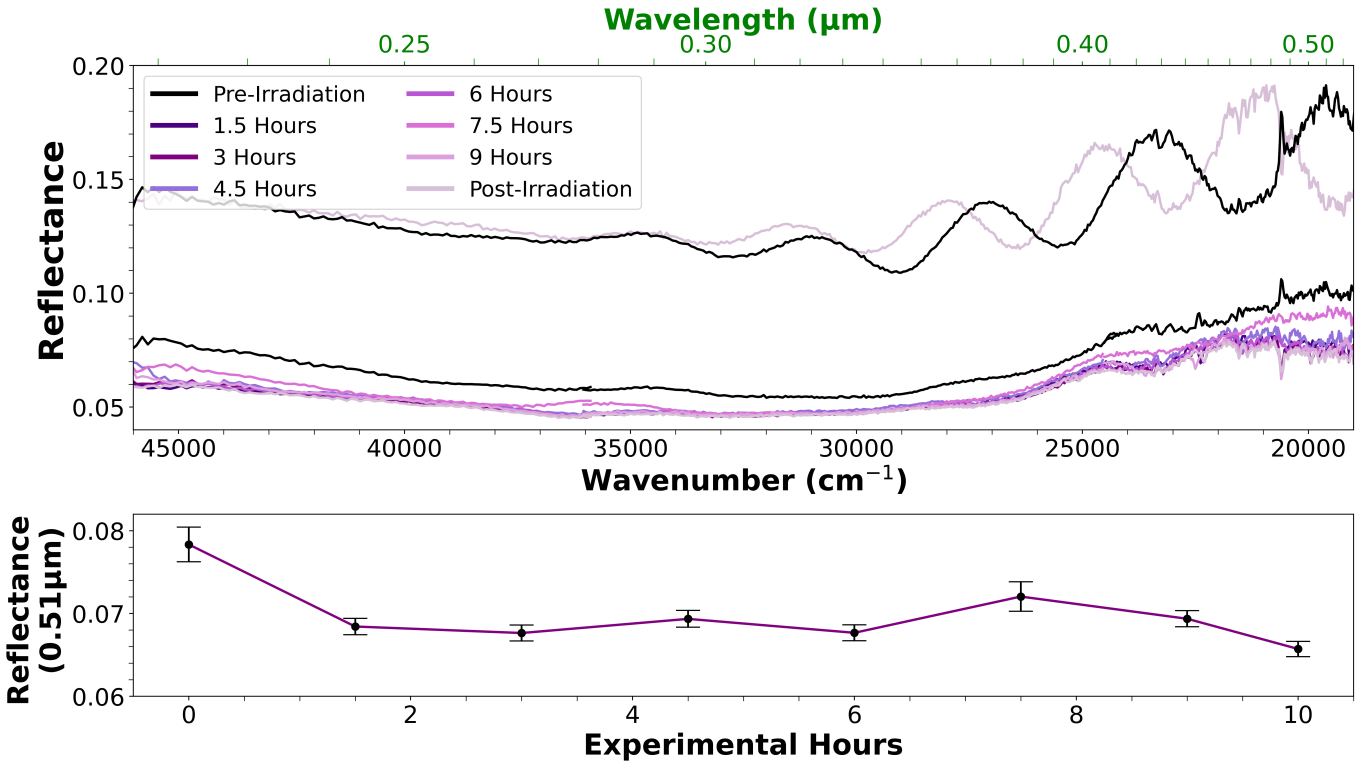

Figure 11. Top: UV-visible (46000 – 18000 cm^{-1}, 0.22 – 0.54 μm) spectrum for the 5% CH_4 atmosphere haze sample across the 240 nm filter. The pre– and post–irradiation uncorrected spectra have been offset vertically 6.5% for clarity. The corrected data during the irradiation process are plotted as is. Bottom: The reflectance of the fringe–corrected data plotted for a specific wavelength (0.51 μm) over the duration of the irradiation process. The error bars for the reflectance changes seen at 0.51 μm are derived from propagating error throughout the instrument and fringe interference equation.

world exoplanet. We also propose that flares that release more energy towards the surrounding planets will decrease the amount of haze present in the planet atmosphere, potentially stripping away not only the haze but the remaining water vapor–dominated atmosphere below.

4. DISCUSSION

So far, the irradiation of Titan–like hazes (e.g., Gavilan et al. 2018) are largely the only source of how haze–like materials react under UV light potentially representative of stellar flaring. Some of the spectral features seen across our laboratory–made hazes are documented throughout the literature (e.g., Hörst & Tolbert 2014; Hörst 2017; Gavilan et al. 2018; He et al. 2022; Moran et al. 2022; He et al. 2024). However, these two concepts have not yet been combined to study the changes in spectral features due to UV irradiation on laboratory–made exoplanet hazes.

This study covers a large wavelength range and provides a comprehensive spectral analysis of laboratory–made exoplanet hazes exposed to UV light. To examine how representative our experiments are to an actual planetary atmosphere experiencing flares, we compare our experimental set–up to a typical flare of an M–dwarf star. The power output of the UV light is 1.1 W/m^2 for a 10 hour time period. The quiescent period radiation of an M dwarf star (e.g., GJ1214) is approximately 3.5 W/m^2. This is a much stronger radiation output than our simulated flare. In addition, flaring energies have significantly more radiation than quiescence, including

harmful UV and X–Ray radiation. The total energy produced by M dwarf flares can be orders of magnitude higher than quiescent energies (e.g., Loyd et al. 2016; Howard et al. 2020). During our simulated flare, we see multiple spectral changes across infrared wavelengths with some larger percent changes (>2%). In addition, the continuum as a whole decreases throughout the UV radiation environment simulated. Therefore, we expect larger changes in both the continuum and specific spectral features noted above in higher–energy UV experiments. This leads to the conclusion that the higher–radiation environment found on water world exoplanets orbiting M dwarfs may be further stripped of their surrounding hazes and water–rich lower atmosphere. This ultimately can leave these exoplanets as bare rocks with total atmospheric loss. This study also provides a baseline for simulated flaring effects on these planet hazes. Future work should include higher–energy lamps if feasible to fully understand the impact that high–energy UV output would have on exoplanet haze degradation.

Our experiments focus on flare energy in the ultraviolet part of the wavelength spectrum. However, flares release energy across a broad wavelength range, which can have more effects on the orbiting planet's atmosphere and haze layer. Stellar activity such as flares temporarily increase the incident flux received by a planet, triggering not only photochemistry but atmospheric escape in the upper layers of the planet's atmosphere. More specifically, the X–ray/extreme ultraviolet (XUV, 100 – 1000Å) wavelength range is a large proponent of atmospheric escape and has the ability to penetrate into the haze layer if the hazes are found in the upper atmospheric layers. This work does not take into account XUV radiation, which may have detrimental results on the longevity of exoplanet hazes. Dissociation in the XUV wavelength region, including H_2, N_2, H_2O, CO, CO_2, and CH_4, occurs shortward of 117 nm (Loyd et al. 2016). All of these molecules are found in the starting composition of our haze samples. By not including XUV radiation in our laboratory experiments, there is potential for much further degradation and dissociation than the results shown here. The photodissociation rates and overall XUV flux in this range will vary between stars, and work understanding the stellar XUV region (e.g., Linsky et al. 2014; Fontenla et al. 2016; Peacock et al. 2019; Duvvuri et al. 2021) in addition to the effects of the XUV region on exoplanet atmospheres (e.g., Howard et al. 2020; Foster et al. 2022; Louca et al. 2023) is already underway and may soon determine how important XUV radiation contributes to the stripping of water world hazes.

Haze production and cycling in an exoplanet atmosphere has the ability to provide an equilibrium from stellar flaring. This study does not take into account the potential for haze production under UV light nor any other haze production mechanism. We assume in this experiment that the representative planetary haze is present and not continuing to grow during the simulated flaring event. Previous laboratory experiments focusing on haze production rates show that they vary widely by composition (e.g., Hörst et al. 2018; He et al. 2018a,b; Moran et al. 2022). This can have varying effects on if the haze would be able to sustain itself over different timescales. Although we did not note the haze production rates, leaving this to a companion paper, the sample including CH_4 atmosphere haze visually produced more haze during the initial haze production process in comparison to the sample including CO. In addition, previous laboratory studies have shown that H_2O–dominated atmospheres produce more haze particles than either H_2– or CO_2–dominated atmospheres (Hörst & Tolbert 2014; Hörst et al. 2018). Therefore, we expect our two sample atmospheres to have higher production rates than other atmospheric hazes. However, the specific physical mechanisms which grow and produce organic haze particles in an exoplanet atmosphere are still largely unknown (e.g., Hörst et al. 2018; He et al. 2020a; Moran et al. 2020; Vuitton et al. 2021). There is potential for a high production rate to reach equilibrium with the haze degradation seen in this study. Alternatively, the radiation provided by the star could strip the haze particles away. However, it remains unclear how this process could be sustained over evolutionary timescales.

Observationally, JWST has a much higher capability of detecting faint spectral features than previous space–based telescopes and can be used to better determine the compositions of exoplanet atmospheres. The hazes that will be observed in the future are expected to be of different compositions, which will have different optical properties. Optical properties are necessary inputs for atmospheric modeling in order to better understand the associated physical and chemical processes at work. This work shows that irradiation of laboratory made exoplanet hazes produces a different spectrum pre– and post–irradiation, which will produce different optical properties. This work paired with future optical constant calculations of these irradiated hazes will be applicable for temperate water world exoplanet atmospheres which orbit closely around their M dwarf host star and are exposed to stellar flaring events.

5. CONCLUSION

In this experiment, we subjected two different water world exoplanet analogue hazes to UV radiation through two different bandpasses of light to determine molecular changes and assess potential haze destruction. Our results show that irradiation alters both the overall continuum and specific spectral features of both the 5% CH_4 and 5% CO atmosphere derived samples. More specifically, the 5% CH_4 atmosphere haze sample exhibits larger overall changes throughout all light bandpasses in both transmittance and reflectance. In addition, the higher–energy representative flare facilitates more overall changes than the lower–energy flare. During the irradiation process in our time-dependent UV-visible wavelengths, we are able to quantify that the hazes lost 1% (320 nm filter) and 1.3% (240 nm filter) of their reflective nature, leading to a thinner haze layer on our representative disks. These laboratory–simulated "flares" have lower energies than most observed M-dwarf flares, which could potentially cause even more aggressive spectral changes than those observed in our experiments. Higher energy flares could lead to higher photodissociation rates, and further atmospheric mass loss around water vapor-dominated exoplanet atmospheres. This increased atmospheric mass loss will affect the climate and ultimately potential habitability of water world exoplanets to a great extent. The results of our first experiment exposing exoplanet hazes to UV radiation provides a better understanding of continuum and spectral feature changes during the irradiation process and how higher–energy irradiation affects the habitability and lifetime of water world exoplanets. More laboratory work is necessary to determine spectral changes of different laboratory–made exoplanet haze compositions. This study provides an avenue in which to determine and quantify spectral changes and resulting compositional properties for future work.

The authors gratefully acknowledge M. S. Marley for supporting this project. We also acknowledge the production of the exoplanet haze analogues by the Johns Hopkins University PHAZER lab, supported by NASA under the XRP program (Grant 80NSSC20K0271), and support by NASA for this study under the SURP program (Grant 2023–048) between the Jet Propulsion Laboratory and the University of Arizona. We also acknowledge NASA grants 80NSSC23K0327, NNX12AL47G, NNX15AJ22G and NNX07AI520, and NSF grants 1531243 and EAR–0841669 for funding of the K-ALFAA facility for the composite images.

REFERENCES

Arney, G., Domagal-Goldman, S. D., Meadows, V. S., et al. 2016, Astrobiology, 16, 873, doi: 10.1089/ast.2015.1422

Arney, G. N., Meadows, V. S., Domagal-Goldman, S. D., et al. 2017, ApJ, 836, 49, doi: 10.3847/1538-4357/836/1/49

Benneke, B., Roy, P.-A., Coulombe, L.-P., et al. 2024, arXiv e-prints, arXiv:2403.03325, doi: 10.48550/arXiv.2403.03325

Benz, A. O., & Güdel, M. 2010, ARA&A, 48, 241, doi: 10.1146/annurev-astro-082708-101757

Borucki, W. J., Koch, D. G., Basri, G., et al. 2011, ApJ, 736, 19, doi: 10.1088/0004-637X/736/1/19

Brande, J., Crossfield, I. J. M., Kreidberg, L., et al. 2024, ApJL, 961, L23, doi: 10.3847/2041-8213/ad1b5c

Corrales, L., Gavilan, L., Teal, D. J., & Kempton, E. M. R. 2023, ApJL, 943, L26, doi: 10.3847/2041-8213/acaf86

Cottrell, T. 1954, The Strengths of Chemical Bonds (Academic Press). https://books.google.com/books?id=7J09AAAAIAAJ

Crossfield, I. J. M., & Kreidberg, L. 2017, AJ, 154, 261, doi: 10.3847/1538-3881/aa9279

Deming, L. D., & Seager, S. 2017, Journal of Geophysical Research (Planets), 122, 53, doi: 10.1002/2016JE005155

Dragomir, D., Benneke, B., Pearson, K. A., et al. 2015, ApJ, 814, 102, doi: 10.1088/0004-637X/814/2/102

Duvvuri, G. M., Pineda, J. S., Berta-Thompson, Z. K., et al. 2021, ApJ, 913, 40, doi: 10.3847/1538-4357/abeaaf

Fontenla, J. M., Linsky, J. L., Garrison, J., et al. 2016, ApJ, 830, 154, doi: 10.3847/0004-637X/830/2/154

Foster, G., Poppenhaeger, K., Ilic, N., & Schwope, A. 2022, A&A, 661, A23, doi: 10.1051/0004-6361/202141097

Fressin, F., Torres, G., Charbonneau, D., et al. 2013, ApJ, 766, 81, doi: 10.1088/0004-637X/766/2/81

Fulton, B. J., Petigura, E. A., Howard, A. W., et al. 2017, VizieR Online Data Catalog, J/AJ/154/109, doi: 10.26093/cds/vizier.51540109

Gao, P., Wakeford, H. R., Moran, S. E., & Parmentier, V. 2021, Journal of Geophysical Research (Planets), 126, e06655, doi: 10.1029/2020JE006655

Gao, P., Thorngren, D. P., Lee, E. K. H., et al. 2020, Nature Astronomy, 4, 951, doi: 10.1038/s41550-020-1114-3

Gavilan, L., Carrasco, N., Vrønning Hoffmann, S., Jones, N. C., & Mason, N. J. 2018, ApJ, 861, 110, doi: 10.3847/1538-4357/aac8df

Grenfell, J. L., Gebauer, S., v. Paris, P., Godolt, M., & Rauer, H. 2014, Planet. Space Sci., 98, 66, doi: 10.1016/j.pss.2013.10.006

Haqq-Misra, J. D., Domagal-Goldman, S. D., Kasting, P. J., & Kasting, J. F. 2008, Astrobiology, 8, 1127, doi: 10.1089/ast.2007.0197

He, C., Horst, S. M., Lewis, N., et al. 2018a, in AAS/Division for Planetary Sciences Meeting Abstracts, Vol. 50, AAS/Division for Planetary Sciences Meeting Abstracts #50, 410.02

He, C., Hörst, S. M., Radke, M., & Yant, M. 2022, PSJ, 3, 25, doi: 10.3847/PSJ/ac4793

He, C., Hörst, S. M., Riemer, S., et al. 2017, ApJL, 841, L31, doi: 10.3847/2041-8213/aa74cc

He, C., Hörst, S. M., Lewis, N. K., et al. 2018b, AJ, 156, 38, doi: 10.3847/1538-3881/aac883

—. 2020a, PSJ, 1, 51, doi: 10.3847/PSJ/abb1a4

—. 2020b, Nature Astronomy, 4, 986, doi: 10.1038/s41550-020-1072-9

He, C., Radke, M., Moran, S. E., et al. 2024, Nature Astronomy, 8, 182, doi: 10.1038/s41550-023-02140-4

Henry, T. J., Jao, W. C., Winters, J. G., et al. 2019, VizieR Online Data Catalog, J/AJ/155/265, doi: 10.26093/cds/vizier.51550265

Hörst, S. M. 2017, Journal of Geophysical Research (Planets), 122, 432, doi: 10.1002/2016JE005240

Hörst, S. M., & Tolbert, M. A. 2014, ApJ, 781, 53, doi: 10.1088/0004-637X/781/1/53

Hörst, S. M., He, C., Lewis, N. K., et al. 2018, Nature Astronomy, 2, 303, doi: 10.1038/s41550-018-0397-0

Howard, W. S., Corbett, H., Law, N. M., et al. 2020, ApJ, 902, 115, doi: 10.3847/1538-4357/abb5b4

Hurford, G. J., Schwartz, R. A., Krucker, S., et al. 2003, ApJL, 595, L77, doi: 10.1086/378179

Jacobson, M. C., Hansson, H. C., Noone, K. J., & Charlson, R. J. 2000, Reviews of Geophysics, 38, 267, doi: 10.1029/1998RG000045

Kasting, J. F., Whitmire, D. P., & Reynolds, R. T. 1993, Icarus, 101, 108, doi: 10.1006/icar.1993.1010

Kite, E. S., & Ford, E. B. 2018, ApJ, 864, 75, doi: 10.3847/1538-4357/aad6e0

Kite, E. S., & Schaefer, L. 2021, ApJL, 909, L22, doi: 10.3847/2041-8213/abe7dc

Knutson, H. A., Benneke, B., Deming, D., & Homeier, D. 2014a, Nature, 505, 66, doi: 10.1038/nature12887

Knutson, H. A., Dragomir, D., Kreidberg, L., et al. 2014b, ApJ, 794, 155, doi: 10.1088/0004-637X/794/2/155

Konings, T., Baeyens, R., & Decin, L. 2022, A&A, 667, A15, doi: 10.1051/0004-6361/202243436

Kreidberg, L., Bean, J. L., Désert, J.-M., et al. 2014, Nature, 505, 69, doi: 10.1038/nature12888

Kreidberg, L., Mollière, P., Crossfield, I. J. M., et al. 2022, AJ, 164, 124, doi: 10.3847/1538-3881/ac85be

Krevelen, D., & Nijenhuis, K. 2009, Optical Properties, 287–318, doi: 10.1016/B978-0-08-054819-7.00010-8

Lavvas, P., & Koskinen, T. 2017, ApJ, 847, 32, doi: 10.3847/1538-4357/aa88ce

Lavvas, P., Yelle, R. V., Koskinen, T., et al. 2013, Proceedings of the National Academy of Science, 110, 2729, doi: 10.1073/pnas.1217059110

Libby-Roberts, J. E., Berta-Thompson, Z. K., Désert, J.-M., et al. 2020, AJ, 159, 57, doi: 10.3847/1538-3881/ab5d36

Lin, C. L., Ip, W. H., Hou, W. C., Huang, L. C., & Chang, H. Y. 2019, ApJ, 873, 97, doi: 10.3847/1538-4357/ab041c

Linsky, J. L., Fontenla, J., & France, K. 2014, ApJ, 780, 61, doi: 10.1088/0004-637X/780/1/61

Louca, A. J., Miguel, Y., Tsai, S.-M., et al. 2023, MNRAS, 521, 3333, doi: 10.1093/mnras/stac1220

Loyd, R. O. P., France, K., Youngblood, A., et al. 2016, ApJ, 824, 102, doi: 10.3847/0004-637X/824/2/102

Luger, R., Barnes, R., Lopez, E., et al. 2015, Astrobiology, 15, 57, doi: 10.1089/ast.2014.1215

Luque, R., & Pallé, E. 2022, Science, 377, 1211, doi: 10.1126/science.abl7164

Madhusudhan, N., Moses, J. I., Rigby, F., & Barrier, E. 2023, Faraday Discussions, 245, 80, doi: 10.1039/D3FD00075C

Marley, M. S., Ackerman, A. S., Cuzzi, J. N., & Kitzmann, D. 2013, in Comparative Climatology of Terrestrial Planets, ed. S. J. Mackwell, A. A. Simon-Miller, J. W. Harder, & M. A. Bullock, 367–392, doi: 10.2458/azu_uapress_9780816530595-ch015

McKay, C. P., Pollack, J. B., & Courtin, R. 1989, Icarus, 80, 23, doi: 10.1016/0019-1035(89)90160-7

—. 1991, Science, 253, 1118, doi: 10.1126/science.11538492

Miguel, Y., Kaltenegger, L., Linsky, J. L., & Rugheimer, S. 2015, MNRAS, 446, 345, doi: 10.1093/mnras/stu2107

Moran, S. E., Hörst, S. M., Vuitton, V., et al. 2020, PSJ, 1, 17, doi: 10.3847/PSJ/ab8eae

Moran, S. E., Hörst, S. M., He, C., et al. 2022, Journal of Geophysical Research (Planets), 127, e06984, doi: 10.1029/2021JE006984

Mordasini, C., Alibert, Y., & Benz, W. 2009, A&A, 501, 1139, doi: 10.1051/0004-6361/200810301

Morley, C. V., Fortney, J. J., Kempton, E. M. R., et al. 2013, ApJ, 775, 33, doi: 10.1088/0004-637X/775/1/33

Moses, J. I., Line, M. R., Visscher, C., et al. 2013, ApJ, 777, 34, doi: 10.1088/0004-637X/777/1/34

Neri, F., Saitta, G., & Chiofalo, S. 1987, Journal of Physics E Scientific Instruments, 20, 894, doi: 10.1088/0022-3735/20/7/015

Ohno, K., & Kawashima, Y. 2020, ApJL, 895, L47, doi: 10.3847/2041-8213/ab93d7

Pavlov, A. A., Brown, L. L., & Kasting, J. F. 2001, J. Geophys. Res., 106, 23267, doi: 10.1029/2000JE001448

Peacock, S., Barman, T., Shkolnik, E. L., Hauschildt, P. H., & Baron, E. 2019, ApJ, 871, 235, doi: 10.3847/1538-4357/aaf891

Pearce, B. K. D., Hörst, S. M., Sebree, J. A., & He, C. 2024, PSJ, 5, 23, doi: 10.3847/PSJ/ad17bd

Rimmer, P. B., Xu, J., Thompson, S. J., et al. 2018, Science Advances, 4, eaar3302, doi: 10.1126/sciadv.aar3302

Rugheimer, S., Kaltenegger, L., Segura, A., Linsky, J., & Mohanty, S. 2015, ApJ, 809, 57, doi: 10.1088/0004-637X/809/1/57

Sánchez-Lavega, A., García-Melendo, E., Pérez-Hoyos, S., et al. 2016, Nature Communications, 7, 13262, doi: 10.1038/ncomms13262

Trainer, M. G., Pavlov, A. A., Dewitt, H. L., et al. 2006, Proceedings of the National Academy of Science, 103, 18035, doi: 10.1073/pnas.0608561103

Vuitton, V., Moran, S. E., He, C., et al. 2021, PSJ, 2, 2, doi: 10.3847/PSJ/abc558

Wilson, E. H., & Atreya, S. K. 2003, Planet. Space Sci., 51, 1017, doi: 10.1016/j.pss.2003.06.003

—. 2004, Journal of Geophysical Research (Planets), 109, E06002, doi: 10.1029/2003JE002181

Wolf, E. T., & Toon, O. B. 2010, Science, 328, 1266, doi: 10.1126/science.1183260

Yu, X., Moses, J. I., Fortney, J. J., & Zhang, X. 2021, ApJ, 914, 38, doi: 10.3847/1538-4357/abfdc7

Zhang, X., Strobel, D. F., & Imanaka, H. 2017, Nature, 551, 352, doi: 10.1038/nature24465